

High pressure redistribution of nitrogen and sulfur during planetary stratification

C.R.M. Jackson, E. Cottrell, Z. Du, N.R. Bennett, Y. Fei

Supplementary Information

The Supplementary Information includes:

- Experimental Methods
- Demonstrations of Equilibrium
- Validation of Predictive Power of Equations 1 and 2
- Further Details for Nitrogen Distribution Model
- Model Results for Other Chondrite Groups
- Tables S-1 to S-3
- Figures S-1 to S-10
- Supplementary Information References

Experimental Methods

We conducted lower *PT* partitioning experiments (1773-2413 K, 0.95-2.38 GPa) using a piston cylinder (PC) and higher *PT* experiments (3046-3437 K, 23.2-25.6 GPa) using a laser-heated diamond anvil (LH-DAC) cell. PC experiments primarily target the effect of temperature, $f\text{O}_2$, X_C^{metal} , X_S^{metal} , and, X_{Ni}^{metal} . LH-DAC experiments target the effect of pressure (*P/T*).

End-loaded, Boyd-style piston cylinder method

We used graphite capsules in all PC experiments loaded with equal weights of silicate oxide power and Fe alloy components. Alloying components include Fe metal, FeSi alloy, FeNi alloy, and Fe-nitride (Fe₂₋₄N). We varied



alloy components to control X_{Ni}^{metal} and experimental fO_2 . The silicate oxide powder composition is basaltic with the exception of experiments designed to test the effect of ionic porosity. Starting silicate compositions were glassed and we report their compositions in Table S-2. We did not include titanium oxide to eliminate the spectral interference of Ti on N during electron microprobe analyses (Speelmanns *et al.*, 2019; Grewal *et al.*, 2019), and we replaced Na with K (by weight) to potentially enable measurements of K partitioning.

We used $BaCO_3$ pressure media, straight-walled graphite furnaces, crushable MgO spacers, and D-type thermocouples in all PC experiments. We machined spacers to position the capsules in the hotspot of the assembly, and we placed a 1 mm MgO disk above the capsule to prevent thermocouple contamination. An Al_2O_3 annulus contained graphite capsules to provide insulation from the furnace, maintain geometry upon compression, and to smooth temperature gradients along the axis of the capsule. We compressed experiments to near the run pressure, ramped by 100 K/min to 1073 K, and annealed for >1 hour to help maintain the integrity of the graphite capsules after melting. We ramped experiments at 150 K/min to the run temperature while maintaining pressure (hot piston in). All experiments were completed at super-liquidus conditions. Power consumption was monitored at the experimental temperatures as a check for thermocouple contamination. We quenched experiments if power consumption started to systematically vary to higher or lower values. Experiments were quenched by cutting the electrical current to the furnace and pressure was held during the quench. Run durations ranged from 1 minute to 3.25 hours, with shorter experiments generally being correspondingly hotter. We assume a 5 % friction correction for PC experiments with $BaCO_3$ pressure media. Temperature uncertainty is assumed to be 10 K and pressure uncertainty is assumed to be 0.05 GPa.

LH-DAC method

LH-DAC experiments constrain the pressure effect on nitrogen partitioning during core formation. Experimental methods follow those outlined in Jackson *et al.* (2018) with several exceptions. Starting materials were a metal-oxide mixture with a bulk composition of C1/C from Thibault and Walter (1995). This mixture was pressed into a sample chamber cut into a preindented Re gasket (~20 μm) using stepped anvils. We then placed foils of MgO



powders above and below the pressed metal+silicate mixture. These foils provide thermal insulation for the heating spots from the diamond anvils and saturate the melt with periclase. Diamond cells with loaded gaskets were then placed in a vacuum oven and heated overnight to remove adsorbed water. Nitrogen was introduced into the DAC by a gas loading system. To ensure a pure N₂ atmosphere was introduced, a vacuum was first drawn and then the gas-loading system was purged with N₂. Gas loading N₂ as the source of nitrogen has the advantage of maintaining a high chemical potential of N₂ throughout the heated spot and adjacent regions. This should limit any tendency for N₂ to continuously diffuse out of the experimental system, as has been observed in lower pressure studies (Speelmanns *et al.*, 2018).

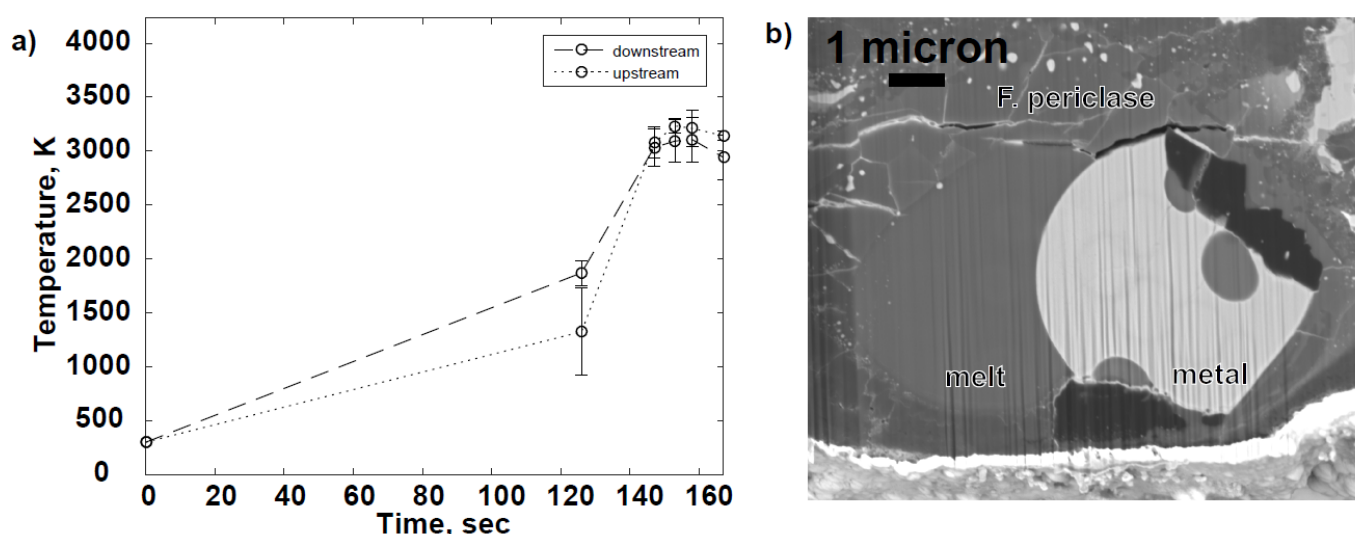


Figure S-1 Representative figures in support of LH-DAC experiments. (a) An example of a time-temperature path for a LH-DAC heating spot (heating spot 2). Both sides of the heating spot (upstream and downstream) were monitored throughout the heating duration. Error bars are the standard deviation of temperature measurement taken in rapid succession. (b) A backscattered image of heating spot 2. The light circle on the right is the quenched alloy and darker regions within the alloy are C-rich. The darker region immediately to the left of the alloy and grey blebs within the alloy are the quenched silicate. The heating spot is surrounded by ferropericlase.

We conducted laser heating at beamline 13-ID-D GSECARS, Advanced Photon Source. Pressure and temperature determinations follow the approach of Jackson *et al.* (2018). Emission spectra were monitored on both sides to constrain the temperature of metal-silicate reaction. Experiment temperatures were determined by fitting emission spectra collected over a 2×2 μm region and taking the average of the hotter side in the final series of measurements prior to quench ($n = 5$ for temperatures above ~3000 K). We take the hotter side as our best estimate of temperature because of the potential for misalignment of the pinhole with the hotspot of the experiment. If present, any misalignment would bias temperature measurements to low values. We quantify temperature by taking the



average of series of measurements immediately prior to quench, and we quantify the temperature stability of LH-DAC experiments by taking the standard deviation of the individual measurements associated with the final temperature measurement series average. A representative time-temperature path is provided in Figure S-1. Pressure is calculated using the equation of state for MgO (Tange *et al.*, 2009) applied at the measured experimental temperature and volume of MgO observed in the experiments, as constrained by x-ray diffraction. Quoted pressure uncertainties include the fractional uncertainty on the temperature, multiplied by the nominal pressure plus an analytical uncertainty of 2 GPa.

An example backscatter electron image and time-temperature path of a LH-DAC experiment are provided in Figure S-1. Quenched metal and silicate phases are well-separated and sufficiently large to enable replicate analyses. The light grey phase is the metallic melt, and the dark grey, angular phases in contact with metallic melt are C-rich, likely diamond. The smooth, intermediate grey phase is quenched silicate melt. The whole heated spot is mantled by ferropericlase.

Sample preparation

PC experimental charges were bisected using a diamond wafering blade and then mounted in epoxy. The cut surface was rough polished with SiC sandpaper using water as the lubricant. Fine polish was achieved using diamond paste with a turbinoid lubricant. Turbinoid, rather than a water-based lubricant, was used during final polishing to limit surface oxidation of the Fe alloy prior to chemical analysis.

A laser cutter was used to liberate the sample chamber of LH-DAC experiments from the remaining gasket. The sample chamber was then loaded onto a TEM grid that was held in place by a custom machined sample post. Heating spots within the sample chamber were exposed for chemical analysis using a focused ion beam (Ga⁺). Final polishing was completed using a 30 kV, 1 nA beam. All samples were Ir coated to facilitate carbon analysis in the Fe alloy phase.



Electron microprobe analysis

Elemental concentrations in glass and Fe alloy phases were determined by electron microprobe analysis (Smithsonian Institution, JEOL 8530F). Standards were as follows: manganite (Mn), diopside (Ca), chromite (Cr), enstatite (Si and Mg), anorthoclase (Al and Na), microcline (K), Fe₅₀Ni₅₀ alloy (Ni), pyrite (S), tungsten carbide (C), silicon nitride (N), iron metal (Fe in metal), augite (Fe in silicate analyses), Re metal (Re). A ZAF matrix correction was used. Analytical conditions were 10 kV, 75-80 nA, and 10 µm diameter electron beam for piston cylinder experiments. Analytical conditions were 10 kV, 5 nA, and 1-3 µm diameter electron beam for LH-DAC experiments. A 10 kV beam was used to minimise matrix corrections on nitrogen as a 10 kV beam creates an activation volume that is relatively close to the surface. An exponential model was used for the nitrogen background to account the curvature local to the nitrogen peak on the LDE1L crystal. Counting times were 90 s on peak and 60 s off peak for nitrogen. The remaining elements were analysed for 30 s on peak and 15 s off peak. Repeat analysis of the basaltic starting composition glass for PC series experiments yields an N concentration of 0.004 ± 0.005 wt. % (Table S-2). Background models for all other elements were linear. All chemical analyses are reported in Table S-1.

Demonstrations of Equilibrium

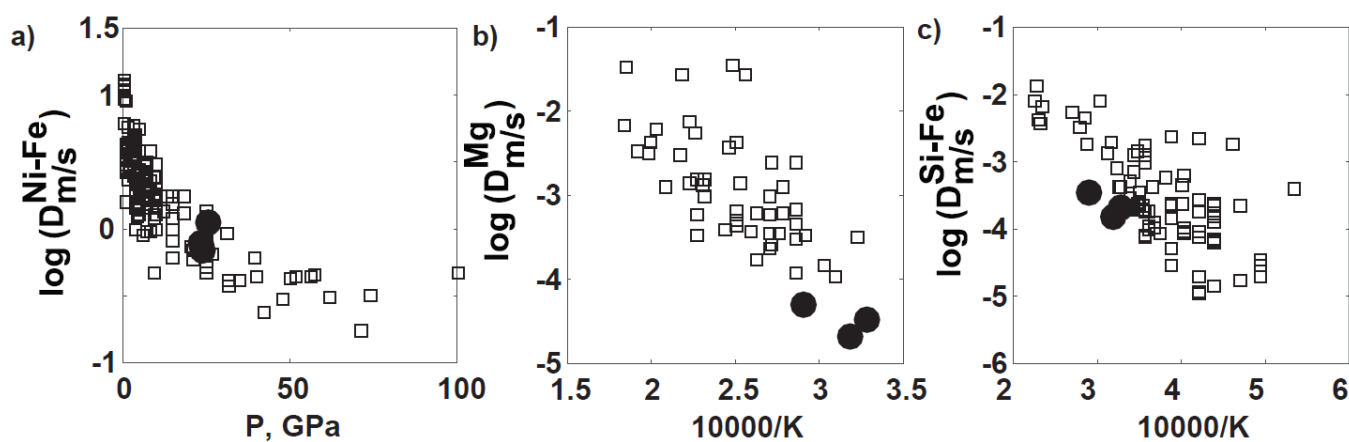


Figure S-2 Comparison of Ni (a), Mg (b), and Si (c) partitioning of LH-DAC experiments (black circles) to literature values (open squares). All data have been recalculated to remove compositional effects using epsilon values from the literature. Ni and Si are plotted as exchange coefficients. Mg is plotted as a disassociation reaction.



We use the partitioning of Ni, Mg, Si between metal and silicate to verify that the LH-DAC experiments closely approached chemical equilibrium for the *P-T* conditions we report (Fig. S-2). This analysis takes advantage of the fact that partitioning of these elements strongly depends on pressure and temperature. We compare our $D_{m/s}^{Ni-Fe}$ data (filled black circles) to the compiled data from Fischer *et al.* (2015) (open squares) in Figure S-2a. All $D_{m/s}^{Ni-Fe}$ data are recalculated to infinite temperature to isolate the effect of pressure using the temperature dependency reported by Fischer *et al.* (2015). We compare our $D_{m/s}^{Mg}$ data to the compiled data from Badro *et al.* (2018) in Figure S-2b. All $D_{m/s}^{Mg}$ data are recalculated to O-, C-, S-, and Si-free metal compositions using the dependencies reported by (Badro *et al.*, 2018) to isolate the effect of temperature. We additionally compare our $D_{m/s}^{Si-Fe}$ data to that compiled in Figure S-2c (Fischer *et al.*, 2015). All $D_{m/s}^{Si-Fe}$ data are recalculated to O-, C-, and N-free metal compositions using the dependencies reported by Fischer *et al.* (2015) (O and C) and (N) (Steelmaking Sourcebook, 1988).

Agreement between our major element partitioning data and the literature data is good for Ni and Mg. Our data do plot on the left edge of the $D_{m/s}^{Si-Fe}$ literature data field. Given the good agreement for the Mg dataset, which suggests accurate temperature measurements, the offset within the Si dataset may suggest 1) minor inaccuracies in the measurement of the low Si content of metals in our experiments and/or 2) underestimation of the effect of C in lowering $D_{m/s}^{Si-Fe}$ values, given the relatively C-rich nature of the metal phases in our experiments (Table 1, Table S-1).

Standard deviations of melt analyses from LH-DAC experiments average 0.038 wt. % N. This value is similar to the average standard deviation of melt from PC series experiments of 0.027 wt. % (Table S-1). Similarly, the average standard deviation of metal analyses from LH-DAC experiments is 0.085 wt. %, which is lower than average of standard deviations from PC experiments of 0.155 wt. %. Standard deviations of PC and LH-DAC experiments are similar. We interpret this to indicate that large-scale N concentration heterogeneities in LH-DAC experiments are not present.

Diffusion length scale provides an additional line of evidence for equilibrium in LH-DAC experiments. The absolute diffusivity of N under the *PT* conditions of LH-DAC experiments is not known, but the relative diffusivity of N in LH-DAC experiments compared to PC experiments can be evaluated by assuming an activation energy of 200



kJ/mol. This value is guided by the combination of results reported by Frischat *et al.* (1978) for the diffusion of N₂ and nitride. Applying an activation energy of 200 kJ/mol and scaling between a temperature of 1973 K (typical of a PC series experiment) and 3100 K (a typical of a LH-DAC series experiment) implies ~100× faster diffusion of N in our LH-DAC experiments compared to PC series experiments. A 100× faster diffusion of N implies a 10× greater diffusion length scale per unit time in our LH-DAC experiments. Given that our LH-DAC experiments are only ~10 μm in diameter, compared to ~1000 μm for a PC experiment, we predict N equilibration should occur ~1000× faster in our LH-DAC experiment. High temperatures are achieved for ~15 seconds in our LH-DAC experiments (Fig S-1b), and this is equivalent to a PC series experiment conducted for 4 hours in terms of the extent of N equilibration. This time is sufficient in PC series experiments to achieve reproducible results and provides an additional line of evidence that LH-DAC experiments closely approached an equilibrium distribution for N.

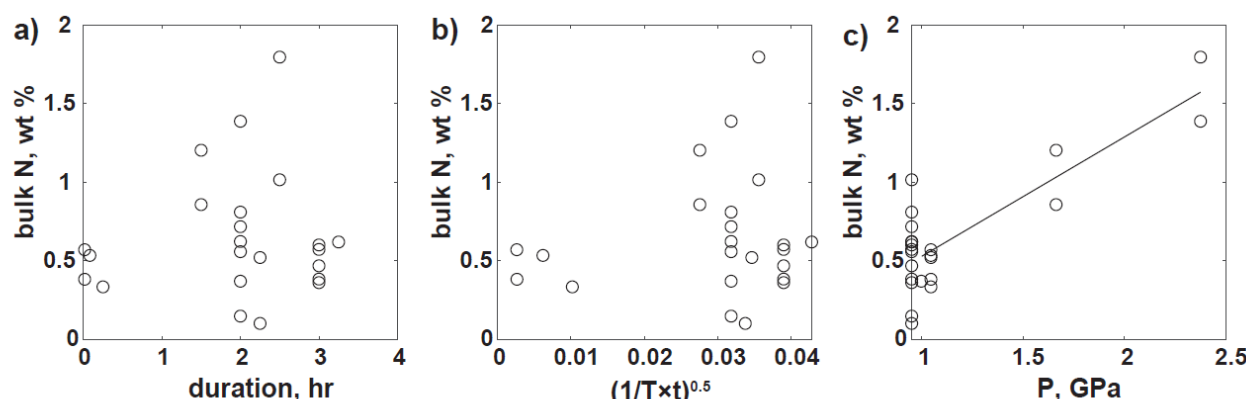


Figure S-3 Evaluation of nitrogen loss from PC experiments. Correlations with duration (a), modified diffusion length scale (b) and pressure (c) with bulk nitrogen concentration of experiments. Correlations are not present in (a) and (b), but bulk nitrogen concentration does correlate with pressure (c) with a p-value 0.05.

Mass balance calculations are not possible for our LH-DAC method. Experiments were gas-loaded with N₂, and laser-heating only melts small regions of the materials loaded into a DAC.

One concern in piston cylinder partitioning experiments is that N can be lost to the surroundings at a rate that causes disequilibrium between metal and silicate. A major line of evidence against N loss being a major factor in our partitioning results is that our temperature and *fO*₂ effect determinations largely agree with previous determinations (*e.g.*, Dalou *et al.*, 2017; Grewal *et al.*, 2019; Speelmanns *et al.*, 2019; Fig. 2).

We can also test directly for N loss by correlating total N content against the duration of the experiment (Fig. S-3a). The data are not correlated, which is consistent with loss not affecting our partitioning results. Nitrogen loss



may be facilitated by a process that is thermally activated. If so, we would expect a correlation between N content and $(1/T \times t)^{0.5}$ (Fig. S-3b). No correlation is present, discounting this possibility.

We calculate bulk N content of experiments using a weighted average of half silicate (N-free) and half metal (N-bearing), following their proportions in our starting materials. All experiments contained metallic powders that are half (by weight) Fe nitride (N content = 7.47 wt. %) for an initial bulk N content of 3.7 wt. % N for each experiment. It is clear that experiments no longer contain the initial N content, but N loss does not appear to affect our partitioning results given our good agreement with previous works (Fig. 2e). One clue regarding the how N is lost comes from the positive correlation we observe between bulk N content and pressure (Fig. S-3c). All our experiments were annealed near their run pressure and 1073 K prior to being ramped to their run temperature. We suggest that the lower bulk N contents of the lower pressure experiments reflect the effect of pressure on the thermal stability of Fe nitride. At atmospheric pressure Fe nitride rapidly decomposes to Fe and N₂ near 773 K (Goodeve and Jack, 1948) and a CO-rich atmosphere, but the volume expansion of this reaction will drive decomposition to higher temperatures at higher pressure. Once decomposition occurs, N₂ gas can leave the system and lower the bulk N content of the lower pressure experiments. It is also possible that the greater compaction of the sample during annealing at higher pressure prevents loss of N₂.

Oxygen fugacity calculation

We calculate $f\text{O}_2$ with respect to the IW buffer using measurements of [Fe] and [FeO] in metal and silicate, respectively, using the following equation (Eq. S-1):

$$\Delta\text{IW} = 2\log(X_{\text{silicate}}^{\text{FeO}} \cdot \gamma_{\text{silicate}}^{\text{FeO}} / X_{\text{metal}}^{\text{Fe}} \cdot \gamma_{\text{metal}}^{\text{Fe}})$$

Activity coefficients for FeO ($\gamma_{\text{silicate}}^{\text{FeO}}$) are calculated according to the parameterisation of O'Neill and Eggins (2002).

We scale $\gamma_{\text{silicate}}^{\text{FeO}}$ calculations for temperature (Eq. S-2):

$$\log(\gamma_{\text{silicate}}^{\text{FeO}})_{T_{\text{experiment}}} = \log(\gamma_{\text{silicate}}^{\text{FeO}})_{T_{1673}} \cdot \frac{1673}{T_{\text{experiment}}}$$



Values of $\gamma_{silicate}^{FeO}$ in mafic and ultramafic systems are near 1, and therefore our temperature scaling has a minimal effect.

Activity coefficients for Fe (γ_{metal}^{Fe}) are calculated following the formalism outlined in Ma (2001) for the interactions between O, S, and C. Interaction parameters are taken from the Steelmaking Sourcebook (1988) with several exceptions. Exceptions are as follows: ε_O^C and ε_O^O values are from Fischer *et al.* (2015) and the ε_O^S value is calculated from the partitioning data of Tsuno *et al.* (2011) ($\varepsilon_O^S = -2.2$).

Parameterisation of non-ideal solution behaviour for nitrogen in liquid Fe-alloy

Our approach to parameterising non-ideal solution behaviour for Fe-alloy follows from recent studies (Fischer *et al.*, 2015; Badro *et al.*, 2018; Jackson *et al.*, 2018). Alloying components in Fe metal alter the solution properties of N with corresponding effects on partitioning. Variations in the solution properties for N are quantified using the activity coefficient of nitrogen dissolved into Fe metal or γ_{Fe}^N . Here γ_{Fe}^N is parameterised following the formalism outlined in Ma (2001), modified to not include the activity coefficient at infinite dilution (γ_N^0) or nitrogen self interaction parameter (ε_N^N) (Eq. S-3):

$$\log(\gamma_{Fe}^N) = \sum \varepsilon_N^i X_{metal}^{\varepsilon i}$$

Where (Eq. S-4)

$$X_{metal}^{\varepsilon i} = T_{ref}/T_{expt.} [X_{metal}^i \left(1 + \frac{\ln(1-X_{metal}^i)}{X_{metal}^i} - \frac{1}{1-X_{metal}^N} \right) - X_{metal}^{i^2} X_{metal}^N \left(\frac{1}{1-X_{metal}^N} + \frac{1}{1-X_{metal}^i} + \frac{X_{metal}^N}{2(1-X_{metal}^N)^2} - 1 \right)]/2.303 \text{ for } i = C, S, \text{ or } Ni$$

Fitting the $1/T$ term in Eq. 1 indirectly accounts for γ_N^0 , and a stepwise fit of partitioning data does not identify ε_N^N as significantly correlated with N partitioning. We assume that $X_{metal}^{\varepsilon i}$ scales with inverse temperature and the reference temperature is 1873 K.



Compositional effects on $D_{m/s}^N$ values

We completed individual series of experiments to quantify compositional controls on nitrogen partitioning. Each series is detailed here.

Carbon-nitrogen interactions in liquid Fe alloy:

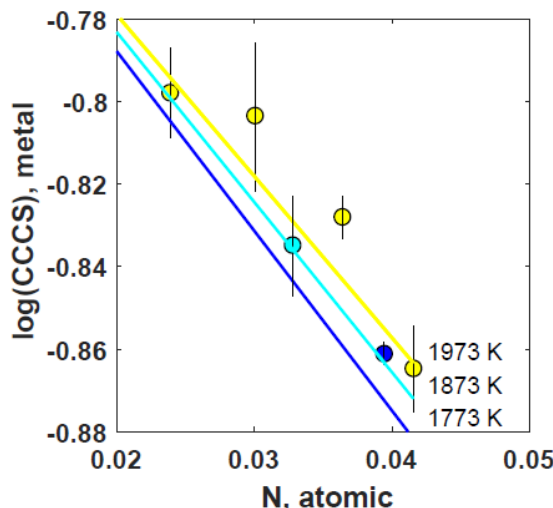


Figure S-4 Correlation between N and C concentration in Fe alloys at graphite saturation (N series). The negative correlation between N and C concentrations indicate that N and C repel each other in liquid Fe alloy. Data points and model lines are color coordinated for their corresponding temperature.

We conducted a series of experiments (N series) with variable X_{metal}^N to quantify the effect of N on C solubility in Fe alloy (Fig. S-4). Measured X_{metal}^C values are treated as solubility because the experiments were completed in graphite capsules, fixing aC to unity. The correlation between X_{metal}^C and $X_{metal}^{\varepsilon N}$ is fit with a ε_N^C value of 7.61 ± 1.41 ($R^2 = 0.90$, p-value = 0.004, n = 6). We make the assumption that C solubility is independent of temperature over the temperature range of the N series (1773–1973 K) given the results of Dasgupta and Walker (2008). The interaction model is given coloured lines, which correspond to the temperature of the experiments in the N series. The fitted data are also plotted with the marker colours that correspond to their temperature.

PTX conditions of the N series are nearly constant at 0.95 GPa, 1773–1973 K, and ΔIW -1.6 to IW-1.8. The negative relationship between carbon solubility and X_{metal}^N is qualitatively consistent with results from the



Steelmaking Sourcebook (1988). We use the ε_N^C value to correct all experiments to a C-free baseline for further fitting using the following equation (Eq. S-5):

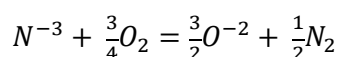
$$\log(D_{m/s}^{N,C\ free}) = \log(D_{m/s}^N) - \varepsilon_N^C \times X_{metal}^{\varepsilon C}$$

We note that the effect of C on $D_N^{m/s}$ values is relatively small in nature if we assume the interaction parameter scales with inverse temperatures and consider reasonable C concentrations in the core. For example, for a core that formed at 3500 K, the inclusion of 1 wt. % C would only lower $D_N^{m/s}$ values by less than a tenth of log unit. Given the uncertainty regarding on core C content (c.f., Dasgupta *et al.*, 2013, Fischer *et al.*, 2020) and its likely small effect, we do not include the effect of C on $D_N^{m/s}$ value in our modelling.

Oxygen fugacity

Oxygen fugacity (fO_2) is a major control on how volatile elements speciate, and each species will have its own unique partitioning behaviour during core formation. We conducted a series of isothermal and isobaric experiments (1973 K and 0.95 GPa) to define the relationship between fO_2 and $D_N^{m/s}$ (Fig. 2a). Data between ΔIW-5 and ΔIW-1 define a positive relationship between fO_2 and $D_N^{m/s}$, where $\log(D_{m/s}^N) \propto 0.64 \pm 0.09\Delta IW$. This individual series correlation coefficient is within error of the coefficient determined for the global regression (0.59 ± 0.04). A similar relationship between fO_2 and $D_{m/s}^N$ has been documented in the literature (Dalou *et al.*, 2017; Grewal *et al.*, 2019; Speelmanns *et al.* 2019).

The role of fO_2 in controlling $D_{m/s}^N$ values can be understood in terms of changes in N solubility within silicate melt. Libourel *et al.* (2003) established that reducing conditions stabilise nitride species in silicate melt, increasing N solubility proportional to $fO_2^{-3/4}$ according with the following reaction (Eq. S-6):



A log coefficient of 0.64 ± 0.09 is within error of the theoretical 0.75 value. A lower than theoretical slope may suggest that deviations from Nernst partitioning, that nitrogen species with an oxidation state intermediate to N₂ and N⁻³ influence melt solubility, or that the speciation of nitrogen is mixed in metal and melt phases.

Under extremely reducing conditions ($<\Delta\text{IW}-5$) there is preliminary evidence for a new $D_{m/s}^N - f\text{O}_2$ regime (Fig. 2a). This shallowing may indicate that nitride species are fully stabilised, such that changes in $f\text{O}_2$ no longer lead to changes in N solubility in silicate melt. Indeed, measurements of nitrogen solubility in silicate liquid below $\Delta\text{IW}-6$ (1 atmosphere and 1698 K) appear to plateau relative to solubility measurements under more oxidised conditions (Libourel *et al.*, 2003).

Effect of nickel and sulfur

We conducted a series of experiments to constrain the effects of Ni and S in modulating $D_{m/s}^N$ values. In the Ni series pressures and temperatures were held constant at 0.95 GPa and 1973 K (Fig. 2b). The individual series correlation yields a ε_N^{Ni} value of 5.32 ± 1.09 ($R^2 = 0.95$, p-value = 0.03, n = 4). This value is within error of those determined in the global regression ($\varepsilon_N^{Ni} = 5.08 \pm 1.42$). A negative effect of Ni on $D_{m/s}^N$ values is qualitatively consistent with literature results (Roskosz *et al.*, 2013) and the Steelmaking Sourcebook (1988).

Within the S series, temperatures varied between 1973 and 2413 K and pressures varied between 0.95 and 2.38 GPa (Fig. 2c). We varied pressure and temperature to provide a greater range of X_{metal}^S values within the S series. The addition of S to Fe alloy makes N less siderophile. Fitting the S series yields a ε_N^S value of 2.08 ± 0.85 ($R^2 = 0.57$, p-value = 0.05, n = 7). Determining the independent effects of S and C is complicated because they are negatively correlated in carbon-saturated systems due to their interactions in metallic melt. A negative effect of S on $D_{m/s}^N$ values is qualitatively consistent with previous partitioning work (Grewal *et al.*, 2019) and the Steelmaking Sourcebook (1988).



Effect ionic porosity

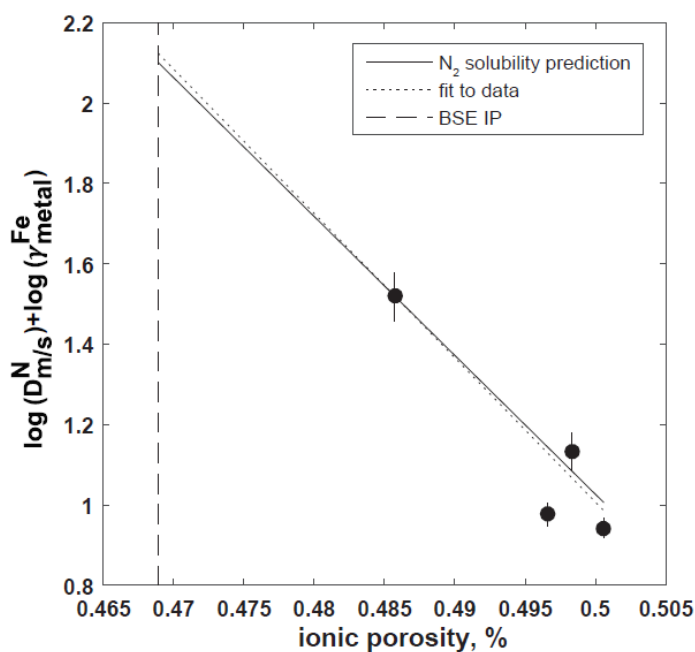


Figure S-5 The effect of ionic porosity of silicate liquid on nitrogen partitioning at 1 GPa and 1973 K. All data have been recalculated to IW-2. The solid line is a least squares fit to the partitioning data, and the dotted line is a model prediction for nitrogen partitioning assuming ionic porosity increases the solubility of N in melt following the established behaviour for Ar (Carroll and Stolper, 1993). The model is forced through the low ionic porosity data point. The vertical dashed line is the ionic porosity for a bulk silicate Earth liquid.

We explored the effect of ionic porosity on $D_{m/s}^N$ values because it is well-established that ionic porosity is a controlling factor on the solubility of neutral species, such as N₂, in silicate melt at low pressure (Fig. S-5). More silica-rich liquids have greater ionic porosity and should consequently have a higher N solubility, provided that N solubility is influenced by neutral species. This behaviour will translate into a higher concentration of N in magma in equilibrium with liquid metal, and a lower $D_{m/s}^N$ value. We test for this effect by completing N partitioning experiments with higher ionic porosity silicate liquids compared to the basaltic liquid used in the remaining piston cylinder experiments. The solubility of N₂ is very similar to Ar in magma due to their equal charge and similar radius, and we use established correlations between Ar solubility and ionic porosity (Carroll and Stolper, 1993) to predict the sensitivity of $\log(D_{m/s}^N) + \log(\gamma_{\text{metal}}^{\text{Fe}})$.



High ionic porosity experiments do have lower corresponding $\log(D_{m/s}^N) + \log(\gamma_{metal}^{Fe})$ (recalculated to carbon free baseline and to ΔIW -2), and the magnitude of the effect is indistinguishable from the prediction made on the basis of Ar solubility. These experiments provide preliminary evidence that ionic porosity modulates $D_{m/s}^N$ values and that N₂, or another neutral species, are significant components of N solubility in the ionic porosity series. Magma oceans have low ionic porosity related to their ultramafic composition, but extrapolating this effect from our 1 GPa experiments to deep magma oceans, however, is difficult due to the collapse of melt structure with pressure. We do not include this effect in Equation 1 for this reason.

The apparent influence of both ionic porosity and fO_2 on $D_{m/s}^N$ values suggests that N speciation in PC series experiments is in a mixed regime where both nitride and neutral species contribute to melt solubility under the conditions explored. The stability of nitride in melt is also suggested by solubility and spectroscopic evidence (Libourel *et al.*, 2003; Mosenfelder *et al.*, 2019; Grewal *et al.*, 2020), and recent work has established that nitride-complexes are more soluble in depolymerised melt (Boulliung *et al.*, 2020).

Validation of Predictive Power of Equations 1 and 2

We combine the individual series ($1/T$, P/T , X_{metal}^{Ni} , X_{metal}^S , ΔIW) into a global dataset and conduct a multiple least squares regression to predict $D_{m/s}^{N,C\ free}$ values up to the PT conditions associated with average core formation within Earth (Eq. 1). We note that in the absence large amounts of alloying elements, $\log(\gamma_{metal}^{Fe})$ value are near zero.

To evaluate the predictive power of Equation 1, we compare $D_{m/s}^N$ reported in the literature to values predicted for the associated experimental conditions and chemical analyses (Fig. S-6). Literature data were collected over a relatively wide range of conditions: 1523 to 2800 K, 0.85 to 14.8 GPa, -0.3 to -5.9 ΔIW). All literature $D_{m/s}^N$ values are recalculated to a carbon-free baseline (Eq. S-5), and then we apply Equation 1 to their corresponding experimental conditions to predict the $D_{m/s}^N$ value for the experiment. Roskosz *et al.* (2013) did not analyse for carbon in their experiments, and in response, we take the analytical total deficit of the metal phase analysis as the carbon concentration.



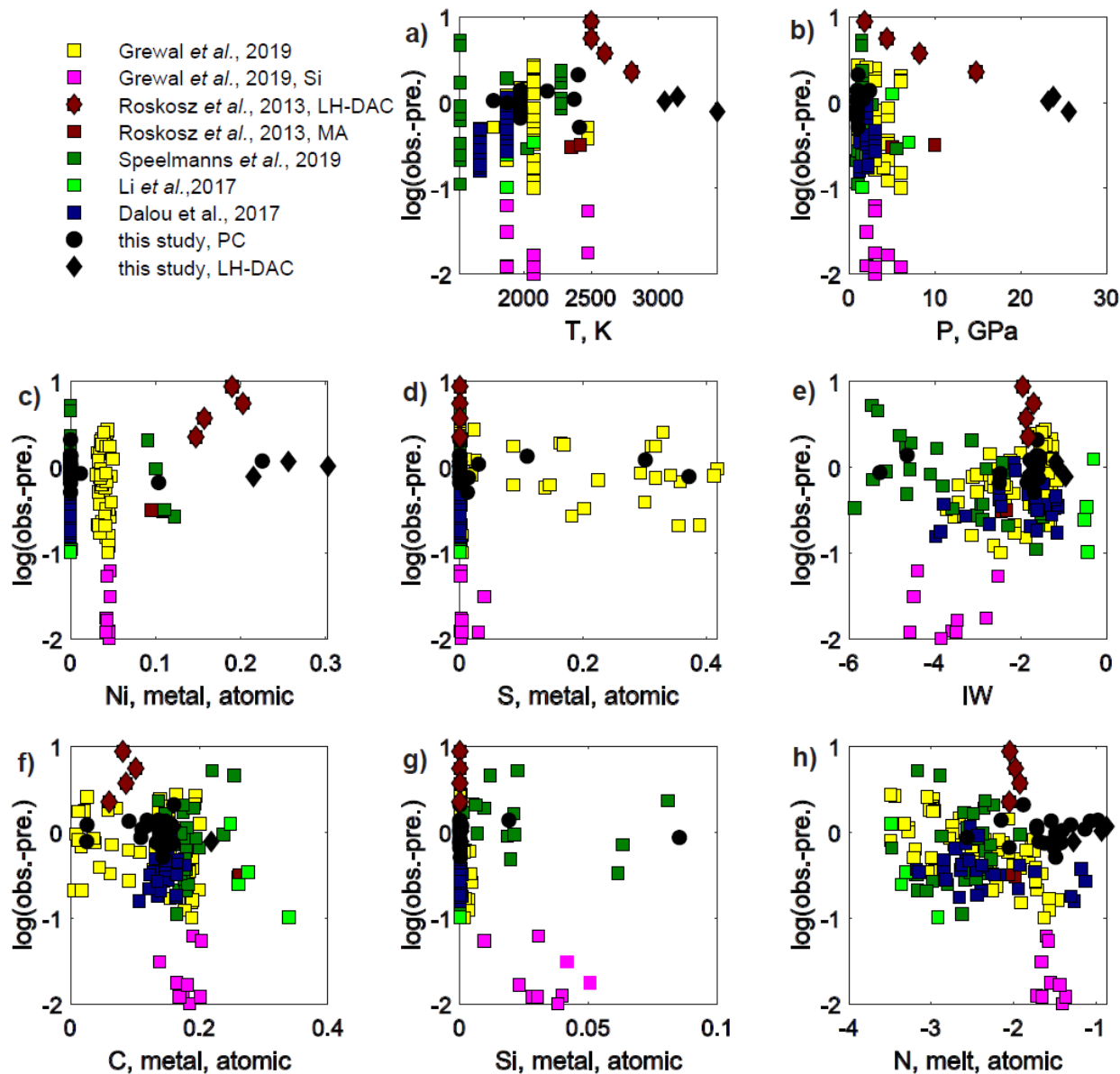


Figure S-6 Comparison of nitrogen partitioning predicted by Eq. 1 and literature observations. **a-e)** Model residuals for Eq. 1 parameters. **f-h)** Model residuals for carbon concentration in metal, silicon concentration in metal, and nitrogen concentration in melt. All data have been recalculated to a C-free baseline.

We plot model residuals to identify systematic inaccuracies in our model predictions or any missing model parameters. There are limited higher pressure data to constrain the effect of pressure on $D_{m/s}^N$ values (Fig. S-6b). The multi-anvil data of Roskosz *et al.* (2013) are the highest pressure multi-anvil data yet reported, and these data are well-explained by the Equation 1. Roskosz *et al.* (2013) also report LH-DAC data that range between 1.8 to 14.8 GPa, and these data are systematically under predicted by our model. The disagreement is largest at low pressure, but this is the



pressure range where $D_{m/s}^N$ values are relatively well-established. Indeed, LH-DAC experiments are typically not attempted at such low PT conditions because they have inherently larger uncertainties in their experimental conditions compared to piston cylinder or multi-anvil approaches. With increasing PT conditions, the LH-DAC data of Roskosz *et al.* (2013) are progressively better predicted by our model, such that their highest PT data are in reasonably well-predicted. Part of the under prediction of the Roskosz *et al.* (2003) LH-DAC data at lower PT conditions may relate to our reliance on total deficits to estimate the carbon content of the metal phases.

We exclude the experiments from Grewal *et al.* (2019) that contain Si in the alloy (>0.5 wt. %). The Si-bearing experiments from Grewal *et al.* (2019) show systematic deviations from our model predictions that correlate with the concentration of Si in the metal (Fig. S-6g). These same deviations are not observed in either the Si-bearing experiments of Speelmanns *et al.* (2019) or of the present study.

Comparing model predictions to the literature yields an R^2 value of 0.76. We stress that we simply predict the literature data, as Equation 1 was derived only from the experiments reported here, rather than fit to the literature data. Fitting the literature dataset (excludes Si-bearing experiments of Grewal *et al.*, 2019) with the same parameters as Equation 1 yields following model ($R^2 = 0.76$, p-value<0.001, n = 127) (Eq. S-7):

$$\log\left(D_{m/s}^{N,C-free}\right) = 3784 \pm 458 1/T + 119 \pm 29 P/T + 1.25 \pm 1.45 X_{metal}^{\varepsilon Ni} + 2.19 \pm 0.48 X_{metal}^{\varepsilon S} + 0.51 \pm 0.02 \Delta IW + 0.48 \pm 0.25 - \log(\gamma_{metal}^{Fe})$$

The pressure and temperature effect parameters of the literature global fit (Eq. S-7) are more moderate compared to Equation 1. The LH-DAC experiments of this study and the Roskosz *et al.* (2013) experiments contain high concentrations of Ni and are crucial for defining the pressure effect (Fig. S-6c). The smaller negative effect of Ni in Equation S-7 compared to Equation 1 therefore serves to lower the pressure effect. Constraining the effect of Ni using the literature dataset is hampered by there being relatively few experiments that systematically vary Ni contents the fact of that the highest pressure experiments also have the high Ni contents (Fig. S-6c). The consequence of a



more moderate pressure effect is somewhat offset by more moderate temperature effect, such that the application of Equation 1 and Equation S-7 to a mantle liquidus geotherm yields less than a half log-unit difference in predicted $D_{m/s}^N$ values at 30 GPa (Fig. S-7). The basic conclusion that $D_{m/s}^N$ values increase with increasing PT conditions is supported by global fitting of the literature dataset.

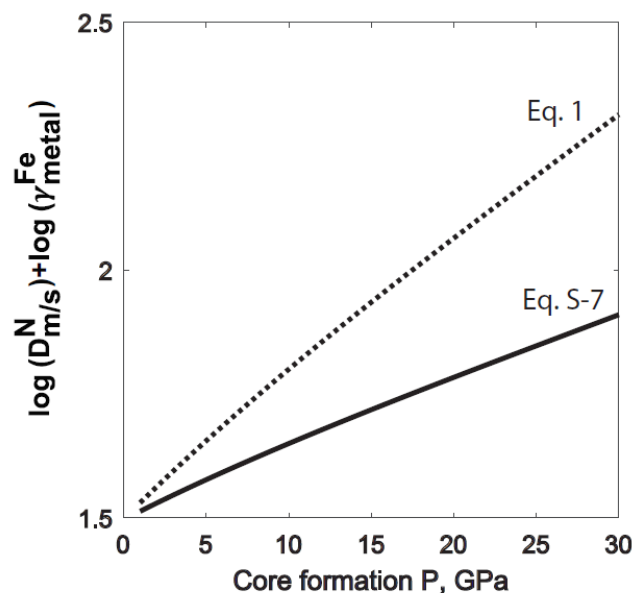


Figure S-7 A comparison of nitrogen partitioning predictions of Eq. 1 and Eq. S-7. Both models predict that nitrogen becomes more siderophile with increasing pressure along a mantle liquidus geotherm, but Eq. 1 predicts approximately twice the rise in partition coefficient between 1 and 30 GPa compared to Eq. S-7.

Parameterisation of $D_S^{m/s}$

We take data collected from experiments run over 10 GPa from Rose-Weston *et al.* (2009) and all data from Suer *et al.* (2017), Jackson *et al.* (2018), and Mahan *et al.* (2018) to parameterise $D_{m/s}^S$ values (Fig. S-8). Lower pressure data are not included because their extrapolation to higher $P-T$ values is inconsistent with more newly made observations. Our base model includes a constant term and following variables: $\frac{1}{T}, \frac{P}{T}, \log(aFeO), \log(C_S)$, and $X_{metal}^{\varepsilon C}$. The observation for fitting is $\log(D_{m/s}^S) + \log(\gamma_{metal}^{Fe})$. The C_S term is the sulfur content at sulfide saturation. The $\frac{1}{T}, \frac{P}{T}$ and constant terms are added to the model and a stepwise approach is used to determine if any of the compositional parameters are significant. We identify $X_{metal}^{\varepsilon C}$ as the only significant additional parameter. This fit epsilon parameter is similar to the ε_S^C value from the steelmaking literature. The partitioning of sulfur should also be



affected by the capacity of the silicate liquid to complex with S²⁻ ions. To test if this effect is significant in the current dataset, we introduce the $\log(aFeO)$ and $\log(C_S)$ terms into the stepwise matrix. The coefficients for both terms are negative, as anticipated, but neither is significant (p-values of 0.23 and 0.26, respectively) and are not included in the final model. Our parameterisation is as follows ($R^2 = 0.78$, $n = 36$):

$$\log(D_{m/s}^S) = 3638 \pm 1199 \frac{1}{T} - 53.4 \pm 10.6 \frac{P}{T} + 10.34 \pm 2.01 X_{metal}^{EC} + 1.60 \pm 0.45 - \log(\gamma_{metal}^{Fe})$$

(Eq S-8)

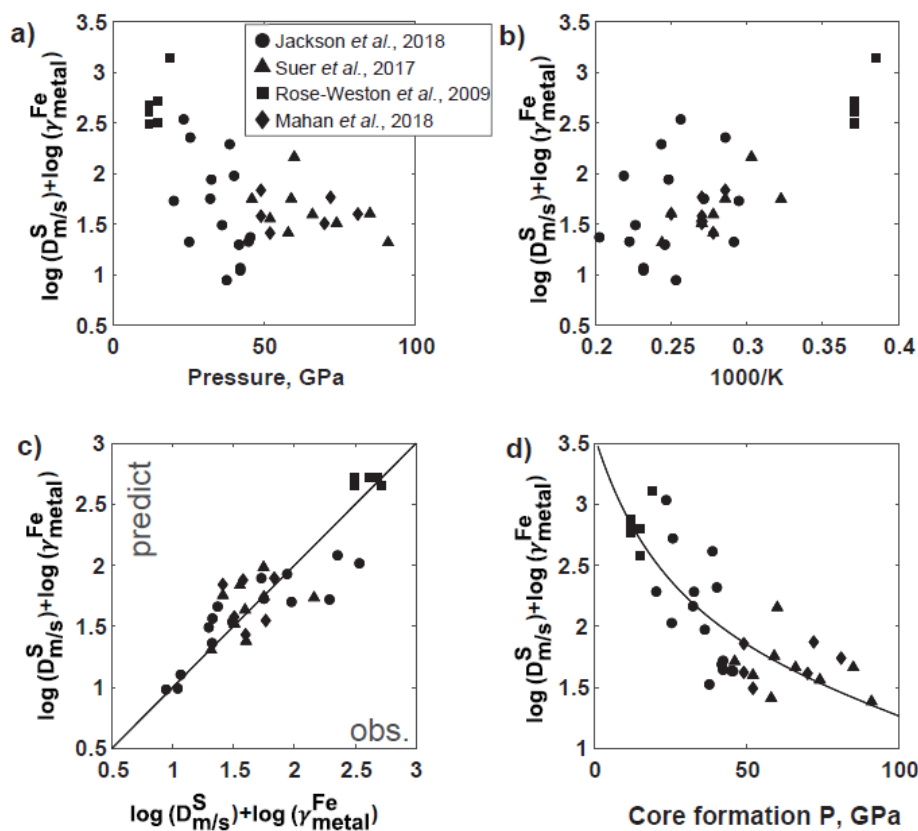


Figure S-8 Parameterisation of S partitioning. Correlations with pressure (a) and inverse temperature (b) used to fit S partitioning parameterization (Eq. S-8). Not shown is the correlation with C content of metal that is also included in Eq. S-8. A comparison of observed and predicted values of S partitioning is plotted in c). Application of Eq. S-8 to the mantle liquidus geotherm is plotted in d). Partitioning data are offset from the model by the difference between their measured value and the value predicted by Eq. S-8. Sulphur is increasingly siderophile with more extreme core formation P - T conditions.



Further Details for N and S Distribution Model

The distribution of N and S are calculated between a primordial atmosphere, magma ocean, and core. For S, we calculate $D_{m/s}^S$ values for each PT condition to calculate the S content of the core assuming 225 ± 25 ppm S in the magma ocean (Hirschmann, 2016). Predicted bulk S contents are plotted in Figures 3e, S-9e, and S-10e. We do not include C and H in our model because, while recent high pressure partitioning data have been published (Fischer *et al.*, 2020; Tagawa *et al.*, 2021), their behaviour remains less well established compared to S (Fig. S-8).

Core formation temperatures are fixed at the mantle liquidus (Fiquet *et al.*, 2010). Predicted bulk S contents are plotted in Figures 3e, S-9e, and S-10e. Low core formation pressures result in high bulk planet S contents because S is relatively siderophile at low pressure. As pressure increases, S becomes less siderophile, and lower bulk S contents are correspondingly predicted. Sulfur is relatively soluble in magma, especially under the more reducing conditions that likely prevail during accretion (O'Neill and Mavrogenes, 2002), and we consequently assume no S is present in the atmosphere. Near 30 GPa, bulk planet S contents match values estimated from Earth's volatility trend (horizontal dotted lines in Figs. 3e, S-9e, and S-10e).

With a bulk planet S content established, we apply S/N ratios from different chondrite groups to calculate bulk N contents. Nitrogen is highly volatile under fO_2 more oxidised than $\Delta IW+0$ (Libourel *et al.*, 2003). We therefore evaluate the distribution of N between the mantle and core, while also including atmosphere. The atmosphere-mantle distribution is constrained by the solubility of N in magma reported by Libourel *et al.* (2003). We convert the solubility relationship so that fO_2 is expressed at ΔIW with the following form (Eq. S-9):

$$N_2^{magma} (\text{mol g}^{-1}) = pN_2 \times (2.2 \times 10^{-9}) + \Delta IW_{atm-mo}^{-\frac{3}{4}} \times 10^{-0.75 \times \Delta IW} \times pN_2^{1/2} \times (1.0 \times 10^{-9})$$

where pN_2 is the partial pressure of N_2 in bar and ΔIW_{atm-mo} is the redox potential of the atmosphere-magma ocean interface, where chemical exchange between these two reservoirs can occur. We chose to use the Libourel *et al.* (2003) study because of its relatively precise determination of N_2 solubility in magma and precise determination of the fO_2 were N solubility transitions from being N_2 - to nitride-dominated.



We allow fO_2 of the atmosphere-magma ocean interface to be different from the core-mantle fO_2 given the evidence for a depth dependence on relationship between fO_2 and Fe^{+3}/Fe_{tot} PT conditions (Zhang *et al.*, 2017; Armstrong *et al.*, 2019) and the temperature dependence on the Fe^{+3}/Fe_{tot} for any given fO_2 (Sossi *et al.*, 2021).

The distribution of nitrogen between magma and core is constrained by the partitioning of N given by Equation 1. We apply these distribution constraints to the following mass balance (Eq. S-10):

$$M_{bulk\ planet}^N = X_{core}^N M_{core} + X_{magma\ ocean}^N M_{magma\ ocean} + X_{atm}^N M_{atm}$$

where M_i denotes masses of reservoirs, X_i^N is the concentration of N in reservoir i , and $M_{bulk\ planet}^N$ is the mass of nitrogen in the bulk planet. Core Ni content is fixed at 5 mol %.

The distribution of N in Earth is mildly sensitive to the bulk N content because below $\sim \Delta IW$ nitrogen dissolves into magma as nitride, while being present in the atmosphere as N_2 . The stoichiometry of this reaction indicates that high concentrations will favour N partitioning into the atmosphere.

The mass of N in the atmosphere is converted to a partial pressure for solubility calculations using the following equation (Eq. S-11):

$$M_{atm}^N = 4\pi p N_2 R^2 / g$$

where R is the radius of the body and g is the acceleration due to gravity for the body.

To complete our mass balance calculations, we must link planet mass to radius and to core formation pressure. Towards this end we first assume an Earth-size planet experiences core formation at 45 GPa with Earth mass and Earth radius. We then scale mass as the cube root of radius and scale core formation pressure as square root of mass. Gravity scales linearly with radius. Our scalings implicitly assume that bulk planet density does not vary with mass. This assumption leads to a marginal over-estimate of gravity acceleration, and therefore a marginal over-estimate for the solubility of N in magma on smaller bodies.

Model Results for Other Chondrite Groups

The S/N ratio of Earth's observable reservoirs (S/N_{OR}) is clearly elevated compared to the gas-rich chondrites that best capture the bulk composition of the Solar System (Fig. 1). Thus, early acting processes preferentially depleted N compared to S in the materials that ultimately comprise the mantle, crust and, and atmosphere of Earth.



An elevated S/N ratio may relate to differentiation processes that preferentially sequester N in the core or to atmospheric loss that preferentially strips away N, as highlighted in our model (Fig. 3).

It is also possible that Earth's elevated S/N_{OR} ratio simply reflects the accretion of relatively S-rich or N-poor materials. Indeed, N contents vary widely between chondrite groups, with decreasing N contents from gas-rich (average of CI and CM) at 1510 ppm, to enstatite at 536 ppm, to ordinary chondrites 54 ppm (Grady *et al.*, 1986; Wasson and Kallemeyn, 1988). Sulfur contents, on the other hand, are relatively constant between chondrite groups, varying from 43000 ppm for gas-rich on the high end to 21667 ppm for ordinary chondrites for the low end. The net effect is that the Solar System produced large variations in the S/N ratio during its earliest evolution, making the S/N ratios of materials that ultimately contributed to Earth's not certain. Here we calculate S/N_{OR} , bulk S content, and bulk N content values for scenarios that first assume bulk planet S/N ratios equal gas-rich chondrites. We then calculate S/N_{OR} , bulk S content, and bulk N content values for scenarios that assume bulk planet S/N ratios equal ordinary chondrites. These models complement those presented in Figure 3 for an enstatite chondrite S/N ratio.

If bulk Earth has a low S/N ratio similar to gas-rich chondrites (29) then differentiation processes must have efficiently depleted Earth's observable reservoirs in N relative to S to raise S/N_{OR} to its current value (81.6 ± 28.5) (Fig. S-9). The differential effect of pressure on S and N partitioning into the core makes high pressure core formation an effective mechanism to drive S/N_{OR} to high values, and our model correspondingly predicts the core formation at 40 GPa can yield Earth-like S/N_{OR} ratio if a reducing atmosphere prevailed ($\sim\Delta IW-3$). More oxidising atmospheres require higher pressures more N remains in the atmosphere, unavailable to partition into the core and low the S/N_{OR} ratio.

If we only consider that the magma ocean contributes to the later observable reservoirs, then the S/N_{OR} constraint is satisfied at ~40 GPa. All cases that consider a bulk planet S/N ratio of gas-rich chondrite require high pressure core formation to drive S/N_{OR} to Earth-like values, and this solution also as the advantage that high pressure core formation also results in bulk Earth S contents similar to estimates derived from Earth's volatility trend (Fig. S-9e). Bulk planet N contents for high pressure scenarios that consider gas-rich chondrite range from 240 to 73 ppm (30-60 GPa).



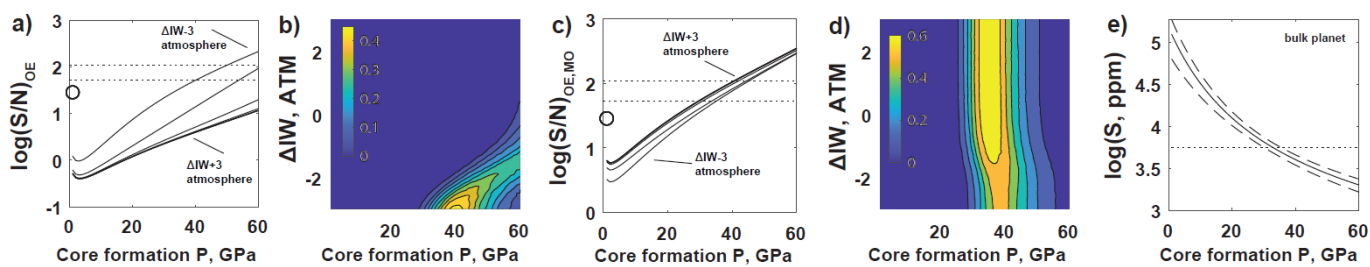


Figure S-9 Equilibrium models for the distribution of S and N. Models take same form as those presented in Figure 3 but assume a bulk planet S/N ratio equal to gas-rich chondrites.

It is also possible that bulk Earth has a high S/N ratio similar to ordinary chondrites (404). In this case, the bulk Earth S/N ratio is higher its S/N_{OR} ratio, and differentiation processes preferentially sequestered S away from its observable reservoirs (Fig. S-10). This is achieved at low pressure, near 10-20 GPa for more reducing atmospheres. These are pressures similar to those inferred for Mars (~15 GPa), a planet that is 1/10th the mass of Earth, and are lower than what single-stage core formation models infer for Earth (*e.g.*, Righter and Drake, 1996; Siebert *et al.*, 2011; Fischer *et al.*, 2015). Low-pressure core formation also makes S relatively siderophile, and implies that Earth is more S-rich than what volatility trends suggest (Fig. S-10e). Such an S-rich planet is not likely, and we discount this scenario. As before, more oxidising atmospheres ($>\Delta IW-1$) require correspondingly higher-pressure core formation to satisfy S/N_{OR} , and allowing for the predicted bulk S content of Earth to match the volatility trend estimates. Only considering the magma ocean as contributing to later observable reservoirs requires low pressure core formation to satisfy Earth's S/N_{OR} ratio, but this scenario also yields an unreasonably high bulk planet S content (Fig. S-10e). We discount this scenario for this reason. Bulk planet N contents for high pressure scenarios that consider ordinary chondrite range from 19 to 6 ppm (30-60 GPa).

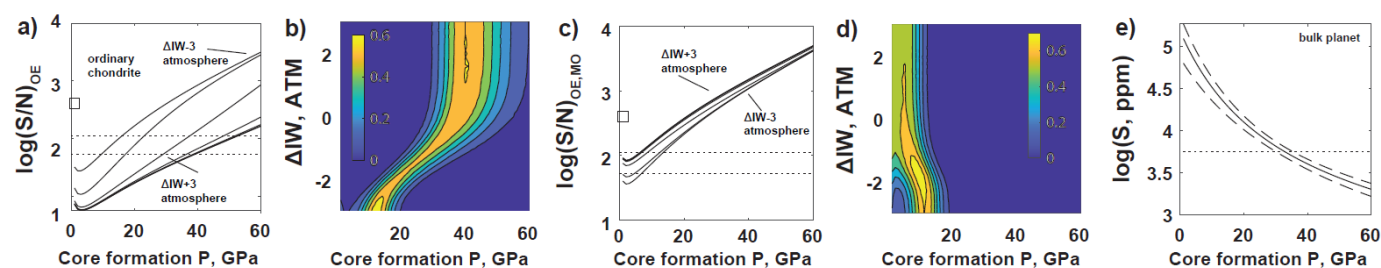


Figure S-10 Equilibrium models for the distribution of S and N. Models take same form as those presented in Figure 3 but assume a bulk planet S/N ratio equal to ordinary chondrites.



We note that our models set the sulfur content of observable reservoirs through metal-silicate reaction at high PT conditions. It is possible that the observable Earth was further depleted in sulfur through the precipitation of a Hadean Matte rich in dense iron-sulfide liquid upon magma ocean crystallisation (O’Neill, 1991). Our model is consistent with the possibility, as core formation at pressures greater than ~30 GPa produces a planet with less than the nominal 5600 ppm S constraint if we assume the magma ocean contains 225 ppm S. Indeed, the relatively low $D_{m/s}^S$ values for S high pressure can leave the magma ocean rich in sulfur (>225 ppm) without violating the bulk planet S constraint (5600 ppm). A Hadean Matte would presumably lower the S/ N_{OE} ratio, but that could be offset by a more oxidising atmosphere or high-pressure core formation (Figs. 3, S-9, S-10). The mass of Hadean Matte allowed in this scenario is several times smaller than what has been previously proposed to satisfy Earth’s budget of highly siderophile elements (Rubie *et al.*, 2016). A large Hadean Matte could be produced if the planet S content constraint is relaxed.

A major message from our modelling is that planetary differentiation processes, through both core formation and atmospheric loss, have major impacts on the volatile budgets of planets. Indeed, our model can reproduce Earth’s S/ N_{OR} ratio across the range of S/N ratios recorded by chondrites by simply varying the pressure of core formation, the atmospheric fO_2 , and the amount of atmospheric loss. In all cases, however, we can only mutually satisfy S/ N_{OR} and bulk planet S constraints if consider core formation pressures similar to those also required to explain refractory elements. Thus, modelling also raises the possibility that Earth’s volatile elements were subjected to the same differentiation events as the rest of the planet – larger planets will redistribute their volatile elements under progressively more extreme PT conditions. This possibility contrasts with the previous suggestion that smaller, highly volatile-rich bodies dominate the delivery of volatiles to Earth (Grewal *et al.*, 2019), effectively decoupling the major physical processes of planetary growth and accretion from major components of habitability. Rather, our suggestion that volatile budgets can be set through the same differentiation events as those robustly recorded by refractory elements implies that volatile budgets, and therefore habitability, are more emergent properties of planets themselves.



Supplementary Tables

Table S-1 Full reporting of experimental conditions (P , T , duration) and chemical analyses of silicate and metal phases.

Table S-2 Chemical analysis of starting materials.

Table S-3 Covariance matrix for Equation 1 (top) and Equation S-8 (bottom).

Tables S-1 to S-3 are available for download (Excel) from the online version of the article at <http://www.geochemicalperspectivesletters.org/article2121>.

Supplementary Information References

- Armstrong, K., Frost, D.J., McCammon, C.A., Rubie, D.C., Ballaran, T.B. (2019) Deep magma ocean formation set the oxidation state of Earth's mantle. *Science*, 903–906.
- Badro, J., Aubert, J., Hirose, K., Nomura, R., Blanchard, I., Borensztajn, S., Siebert, J. (2018) Magnesium partitioning between earth's mantle and core and its potential to drive an early exsolution geodynamo. *Geophysical Research Letters* 45, 13,240-213,248.
- Boulliung, J., Füri, E., Dalou, C., Tissandier, L., Zimmermann, L., Marrocchi, Y. (2020) Oxygen fugacity and melt composition controls on nitrogen solubility in silicate melts. *Geochimica et Cosmochimica Acta* 284, 120-133.
- Carroll, M.R., Stolper, E.M. (1993) Noble gas solubilities in silicate melts and glasses: New experimental results for argon and the relationship between solubility and ionic porosity. *Geochimica et Cosmochimica Acta*, 5039–5051.
- Dalou, C., Hirschmann, M.M., von der Handt, A., Mosenfelder, J., Armstrong, L.S. (2017) Nitrogen and carbon fractionation during core–mantle differentiation at shallow depth. *Earth and Planetary Science Letters*, 141–151.
- Dasgupta, R., Walker, D. (2008) Carbon solubility in core melts in a shallow magma ocean environment and distribution of carbon between the earth's core and the mantle. *Geochimica et Cosmochimica Acta* 72, 4627-4641.
- Dasgupta, R., Chi, H., Shimizu, N., Buono, A.S., Walker, D. (2013) Carbon solution and partitioning between metallic and silicate melts in a shallow magma ocean: Implications for the origin and distribution of terrestrial carbon. *Geochimica Et Cosmochimica Acta* 102, 191-212.
- Fischer, R.A., Nakajima, Y., Campbell, A.J., Frost, D.J., Harries, D., Langenhorst, F., Miyajima, N., Pollok, K., Rubie, D.C. (2015) High pressure metal–silicate partitioning of Ni, Co, V, Cr, Si, and O. *Geochimica et Cosmochimica Acta*, 177–194.
- Fischer, R.A., Cottrell, E., Hauri, E., Lee, K.K., Le Voyer, M. (2020) The carbon content of earth and its core. *Proceedings of the National Academy of Sciences* 117, 8743-8749.
- Fiquet, G., Auzende, A.L., Siebert, J., Corgne, A., Bureau, H., Ozawa, H., Garbarino, G. (2010) Melting of peridotite to 140 gigapascals. *Science* 329, 1516-1518.



- Frischat, G.H., Buschmann, O., Meyer, H. (1978) Diffusion von stickstoff in glasschmelzen, *Glastechn Ber* 51, 321-327.
- Goodeve, C., Jack, K. (1948) Kinetics of nitrogen evolution from an iron-nitrogen interstitial alloy. *Discussions of the Faraday Society* 4, 82-91.
- Grady, M.M., Wright, I., Carr, L., Pillinger, C. (1986) Compositional differences in enstatite chondrites based on carbon and nitrogen stable isotope measurements. *Geochimica et Cosmochimica Acta* 50, 2799-2813.
- Grewal, D.S., Dasgupta, R., Holmes, A.K., Costin, G., Li, Y., Tsuno, K. (2019) The fate of nitrogen during core-mantle separation on Earth. *Geochimica et Cosmochimica Acta*, 87–115.
- Grewal, D.S., Dasgupta, R., Farnell, A. (2020) The speciation of carbon, nitrogen, and water in magma oceans and its effect on volatile partitioning between major reservoirs of the solar system rocky bodies. *Geochimica et Cosmochimica Acta* 280, 281-301.
- Hirschmann, M.M. (2016) Constraints on the early delivery and fractionation of Earth's major volatiles from C/H, C/N, and C/S ratios. *American Mineralogist*, 540–553.
- Jackson, C.R., Bennett, N.R., Du, Z., Cottrell, E., Fei, Y. (2018) Early episodes of high-pressure core formation preserved in plume mantle. *Nature*, 491.
- Li, Y., Marty, B., Shcheka, S., Zimmermann, L., Keppler H. (2016) Nitrogen isotope fractionation during terrestrial core-mantle separation. *Geochemical Perspectives Letters*, 2, 138-147
- Libourel, G., Marty, B., Humbert, F. (2003) Nitrogen solubility in basaltic melt. Part I. Effect of oxygen fugacity. *Geochimica Et Cosmochimica Acta*, 4123–4135.
- Ma, Z. (2001) Thermodynamic description for concentrated metallic solutions using interaction parameters. *Metallurgical and Materials Transactions B*, 87–103.
- Mahan, B., Siebert, J., Blanchard, I., Badro, J., Kubik, E., Sossi, P., Moynier, F. (2018) Investigating earth's formation history through copper and sulfur metal-silicate partitioning during core-mantle differentiation. *Journal of Geophysical Research: Solid Earth* 123, 8349-8363.
- Mosenfelder, J.L., Von Der Handt, A., Füri, E., Dalou, C., Hervig, R.L., Rossman, G.R., Hirschmann, M.M. (2019) Nitrogen incorporation in silicates and metals: Results from SIMS, EPMA, FTIR, and laser-extraction mass spectrometry. *American Mineralogist* 104, 31-46.
- O'Neill, H.S.C. (1991) The origin of the moon and the early history of the earth—a chemical model. Part 2: The Earth. *Geochimica et Cosmochimica Acta* 55, 1159-1172.
- O'Neill, H.S.C., Eggins, S.M. (2002) The effect of melt composition on trace element partitioning: An experimental investigation of the activity coefficients of FeO, NiO, CoO, MoO₂ and MoO₃ in silicate melts. *Chemical Geology* 186, 151-181.
- O'Neill, H.S.C., Mavrogenes, J.A. (2002) The sulfide capacity and the sulfur content at sulfide saturation of silicate melts at 1400 °C and 1 bar. *Journal of Petrology* 43, 1049-1087.
- Righter, K., Drake, M.J. (1996) Core formation in Earth's moon, Mars, and Vesta. *Icarus*, 513–529.
- Rose-Weston, L., Brenan, J.M., Fei, Y., Secco, R.A., Frost, D.J. (2009) Effect of pressure, temperature, and oxygen fugacity on the metal-silicate partitioning of Te, Se, and S: Implications for earth differentiation. *Geochimica et Cosmochimica Acta* 73, 4598-4615.
- Roskosz, M., Bouhifd, M.A., Jephcoat, A.P., Marty, B., Mysen, B.O. (2013) Nitrogen solubility in molten metal and silicate at high pressure and temperature. *Geochimica Et Cosmochimica Acta*, 15–28.



- Rubie, D.C., Laurenz, V., Jacobson, S.A., Morbidelli, A., Palme, H., Vogel, A.K., Frost, D.J. (2016) Highly siderophile elements were stripped from earth's mantle by iron sulfide segregation. *Science* 353, 1141-1144.
- Siebert, J., Corgne, A., Ryerson, F.J. (2011) Systematics of metal–silicate partitioning for many siderophile elements applied to Earth's core formation. *Geochimica et Cosmochimica Acta*, 1451–1489.
- Sossi, P.A., Burnham, A.D., Badro, J., Lanzirotti, A., Newville, M., O'Neill, H.S.C. (2020) Redox state of Earth's magma ocean and its Venus-like early atmosphere. *Science advances*, eabd1387.
- Speelman, I.M., Schmidt, M.W., Liebske, C. (2018) Nitrogen solubility in core materials. *Geophysical Research Letters* 45, 7434-7443.
- Speelman, I.M., Schmidt, M.W., Liebske, C. (2019) The almost lithophile character of nitrogen during core formation. *Earth and Planetary Science Letters*, 186–197.
- Steelmaking Data Sourcebook* (1988) The Japan Society for the Promotion of Science: The 19th Committee on Steelmaking, Gordon and Breach Science Publishers, New York.
- Suer, T-A., Siebert, J., Remusat, L., Menguy, N., Fiquet, G. (2017) A sulfur-poor terrestrial core inferred from metal–silicate partitioning experiments. *Earth and Planetary Science Letters* 469, 84-97.
- Tagawa, S., Sakamoto, N., Hirose, K., Yokoo, S., Hernlund, J., Ohishi, Y., Yurimoto, H. (2021) Experimental evidence for hydrogen incorporation into earth's core. *Nature communications* 12, 1-8.
- Tange, Y., Nishihara, Y., Tsuchiya, T. (2009) Unified analyses for P-V-T equation of state of MgO: A solution for pressure-scale problems in high P-T experiments. *Journal of Geophysical Research: Solid Earth* 114(B3) doi: 10.1029/2008JB005813.
- Thibault, Y., Walter, M.J. (1995) The influence of pressure and temperature on the metal-silicate partition coefficients of nickel and cobalt in a model c1 chondrite and implications for metal segregation in a deep magma ocean. *Geochimica et Cosmochimica Acta* 59, 991-1002.
- Tsuno, K., Frost, D.J., Rubie, D.C. (2011) The effects of nickel and sulphur on the core–mantle partitioning of oxygen in earth and mars. *Physics of the Earth and Planetary Interiors* 185, 1-12.
- Wasson, J.T., Kallemeyn, G.W. (1988) Compositions of chondrites. *Philosophical Transactions of the Royal Society of London. Series A, Mathematical and Physical Sciences*, 535–544.
- Zhang, H., Hirschmann, M., Cottrell, E., Withers, A. (2017) Effect of pressure on Fe³⁺/ΣFe ratio in a mafic magma and consequences for magma ocean redox gradients. *Geochimica et Cosmochimica Acta*, 83–103.

